universe

MDPI

Article

Extremely Metal-Poor Asymptotic Giant Branch Stars

Mario Cirillo [1,2,†], Luciano Piersanti [1,3,†] and Oscar Straniero [1,4,*,†]

[1] INAF-Osservatorio Astronomico d'Abruzzo, Via Mentore Maggini snc, 64100 Teramo, Italy; mario.cirillo@inaf.it (M.C.); luciano.piersanti@inaf.it (L.P.)
[2] Physics Department, Università di Roma Tor Vergata, Via Cracovia, 50, 00133 Roma, Italy
[3] Istituto Nazionale di Fisica Nucleare, Sezione di Perugia, Via Pascoli, 06121 Perugia, Italy
[4] Istituto Nazionale di Fisica Nucleare, Sezione di Roma, Piazzale Aldo Moro, 2, 00185 Roma, Italy
* Correspondence: oscar.straniero@inaf.it
† These authors contributed equally to this work.

Abstract: Little is known about the first stars, but hints on this stellar population can be derived from the peculiar chemical composition of the most metal-poor objects in the Milky Way and in resolved stellar populations of nearby galaxies. In this paper, we review the evolution and nucleosynthesis of metal-poor and extremely metal-poor (EMP) stars with low and intermediate masses. In particular, new models of 6 $M_\odot$ with three different levels of metallicity, namely $Z = 10^{-4}$, 10^{-6} and 10^{-10}, are presented. In addition, we illustrate the results obtained for a 2 $M_\odot$, $Z = 10^{-5}$ model. All these models have been computed by means of the latest version of the FuNS code. We adopted a fully coupled scheme of solutions for the complete set of differential equations describing the evolution of the physical structure and the chemical abundances, as modified by nuclear processes and convective mixing. The scarcity of CNO in the material from which these stars formed significantly affects their evolution, their final fate and their contribution to the chemical pollution of the ISM in primordial galaxies. We show the potential of these models for the interpretation of the composition of EMP stars, with particular emphasis on CEMP stars.

Keywords: stars: population III; stars: evolution; stars: abundances; nucleosynthesis

Citation: Cirillo, M.; Piersanti, L.; Straniero, O. Extremely Metal-Poor Asymptotic Giant Branch Stars. *Universe* **2022**, *8*, 44. https://doi.org/10.3390/universe8010044

Academic Editor: Sylvia Ekström

Received: 12 December 2021
Accepted: 5 January 2022
Published: 11 January 2022

1. Introduction

The oldest stellar component of the Milky Way, i.e., the stars belonging to the galactic halo, covers a rather large range of under-solar metallicities. If the most metal-poor Globular Clusters have $[Fe/H] \sim -2.3$, which roughly corresponds to $Z = 0.0001$, a few field stars with even lower metallicity, namely [Fe/H] down to ~ -7 (or $Z \approx 10^{-9}$), have been discovered so far. These EMP stars ($[Fe/H] \lesssim -2.3$) are less than 2% of the whole halo stellar population (see, e.g., [1,2]), but they are expected to bring the chemical imprint of the first stellar population, the so-called population III (pop III), likely born in small protogalaxies or minihalos of $\sim 10^6$ $M_\odot$ [3]. For this reason, EMP stars were (and are) the objective of several dedicated surveys.

In spite of the many efforts made so far, several unanswered questions still remain about the physical processes that governed stellar birth in the early Universe. One of the most intriguing issues about pop III stars concerns their initial mass function. According to the Big Bang nucleosynthesis calculations, the gas from which the first stars were formed was a mixture of H and He (mass fractions $X = 0.75$ and $Y = 0.25$, respectively) with a negligible amount of other light elements. Under this peculiar condition, the star formation process is expected to proceed differently. It has been recognized early that a successful star formation process requires an efficient radiative cooling mechanism, which drives the collapse of gas clouds towards a sufficiently high density. Owing to the lack of heavy elements, the most important cooler in primordial gas was molecular hydrogen, H_2 (see, e.g., [4,5]). Based on extant models, the first stars are expected to be very massive and short-lived (just a few Myr). This scenario seems to be confirmed by the scarcity of EMP stars

in the Milky Way halo, and, more generally, in the resolved stellar populations of nearby galaxies. However, as first suggested by [6], under certain conditions, hydrogen deuteride, HD, instead of H_2, may become the most efficient cooler. In practice, the activation of the HD cooling lowers the characteristic gravitational fragmentation mass scale and may also reduce the accretion rate of gas onto the protostar seeds [6–8]. As a result, lower mass stars should form. According to this scenario, pop III should include two different generations of stars: a first generation essentially made of massive or very massive stars and a second generation, whose mass function is peaked in the low/intermediate mass region (between 1.5 and 7 $M_\odot$). Note that, although the lifetimes of second-generation stars were definitely longer than those of the first generation, they could have had enough time to pollute the gas from which the Milky Way halo stars formed.

In any case, hints about the pop III mass distribution may be indirectly obtained by analyzing the composition of EMP objects in our Galaxy or in other resolved stellar populations. As usual for halo objects, EMP stars show a significant overabundance of α elements, such as O, Mg or Ca, as well as enhancements of heavy elements produced by the rapid neutron capture nucleosynthesis (r-process), such as Eu. In addition, a lack of heavy elements produced by the slow neutron capture nucleosynthesis (s-process) is generally found, except for a few interesting cases. Both α- and r-enhancements are expected to be the result of early pollution from massive stars, some of which exploded as core-collapse supernovae. On the contrary, isotopes belonging to the main component of the s-process are synthesized by low-mass Asymptotic Giant Branch (AGB) stars (between 1.5 and 3 $M_\odot$). More intriguingly, an important fraction of EMP stars are carbon-rich. These stars are also called CEMP, or Carbon-Enhanced Metal-Poor, stars. Some of them present r-process enrichments (CEMPr), while others are s-process rich (CEMPs). The problem is that most of the carbon in the solar system ($\sim$80%) has been produced by a previous generation of low-mass AGB stars [9], the same objects responsible for the synthesis of the bulk of the s-process isotopes. Indeed, CEMPs stars are believed to be secondary components of binary systems in which the primary star is evolved up to the white dwarf cooling sequence, and part of its envelope is transferred to the secondary by Roche lobe overflow or wind accretion when it was an AGB star [10]. Obviously, this scenario does not work for CEMPr stars because of the lack of s-process isotopes. A possible explanation may be that in these stars, the C enrichment is the result of sub-luminous core-collapse supernovae. These explosions do not produce enough energy to eject all the material surrounding the collapsed core, so the most internal iron-rich layer falls back to the central compact remnant, while the more external layers, in particular, the region where carbon has been synthesized by the hydrostatic He burning, are ejected. Hence, the ejecta of these fallback supernovae should be characterized by high (C/Fe) ratios. Note that the lack of s-process elements does not exclude a contribution from intermediate-mass stars ($5 < M/M_\odot < 9$). These stars experience an AGB (or super-AGB) phase, but at variance with low-mass AGB stars, the neutron sources are not very efficient, and the third dredge-up (TDU) is shallower so that the convective envelope barely penetrates the H-exhausted core. Therefore, the s-process enhancement may be negligible. Nonetheless, the wind generated by these AGB stars is enriched in C+N+O. Indeed, the CNO cycle cannot be active in a H-burning shell of metal-deficient pop III stars, unless some primary CNO is locally produced. Hence, the H burning is initially driven by the pp chain, but, in order to release enough nuclear energy, the local temperature should be much higher than that required in the case of CNO burning. Then, the local temperature increases until the 3α reactions begin producing some C, and, when enough C is accumulated, the CNO cycle eventually starts. As a result, the primary carbon previously synthesized by the 3α reactions is redistributed into the various stable isotopes of C, N and O. Eventually, this CNO-enhanced material is diluted in the convective envelope by the various dredge-up episodes occurring during the Red Giant Branch (RGB) and AGB phases (see, e.g., [11]). Since the lifetime of these stars is of the order of 20–60 Myr, if the pop III mass function extends down to the intermediate mass range, the imprints of their pollution may be found in some EMP stars.

The present work is focused on the peculiar evolution and nucleosynthesis of metal-deficient low- and intermediate-mass stars. All the computations here presented have been performed by means of the latest version of the FuNS code [12–14]. Our code allows us to choose different degrees of coupling between the equations governing the physical structure and those describing the chemical evolution due to nuclear burning and mixing induced by convective instabilities. For the models discussed in this work, we have adopted a scheme in which all the equations are solved simultaneously (see also [15]). This is a necessary condition to properly account for the reciprocal feedback occurring in all the cases in which a convective zone extends into a region of variable composition, so fresh nuclear fuel is moved to a higher temperature where nuclear reactions proceed at a faster rate. These episodes are expected to be quite common in pop III and EMP stars. Although several theoretical studies on EMP stars have been previously conducted [11,16–20], this is the first time that metal-deficient intermediate-mass models have been computed with a fully coupled scheme. Since this computational scheme is time-consuming, we have selected a nuclear network limited to the processes that produce a major contribution to the nuclear energy release. It includes 30 isotopes and 68 reactions (both strong and weak interactions). Mixing by convection is treated as an advection process rather than a diffusive one. The other physics inputs are as in [14]. Rotation is not considered here.

In Section 2, we will compare models of 6 $M_\odot$ computed with three different initial metallicities, namely 10^{-4}, 10^{-6} and 10^{-10}. Then, a model of 2 $M_\odot$, $Z = 10^{-5}$ is illustrated in Section 3. Final remarks follow.

2. Massive AGB Stars

In this section, we discuss the differences between three models with same initial mass (6 $M_\odot$) and He mass fraction ($Y = 0.25$) but different metallicity, namely $Z = 10^{-4}, 10^{-6}$ and 10^{-10}.

2.1. H- and He-Burning Phases

In Table 1, we report the duration of the Pre-Main Sequence, core-H burning and core-He burning for the three 6 $M_\odot$ models. A reduction in the major burning lifetimes can be noticed as the metallicity decreases.

Table 1. Duration of the main phases of the three models.

Z	Pre-Main Sequence (Myr)	Central-H Burning (Myr)	Central-He Burning (Myr)
10^{-4}	0.329	47.5	8.70
10^{-6}	0.436	43.5	8.62
10^{-10}	0.626	38.1	6.37

After the Pre-Main Sequence phase, H burning settles near the center of the star and a convective core develops, whose extension in mass is shown in Figure 1. In the $Z = 10^{-4}$ and $Z = 10^{-6}$ models, H is converted into He through the CNO cycle. The radiative opacity, mainly due to electron scattering, and thus proportional to hydrogen abundance, decreases, resulting in a gradual shrinkage of the convective core. When the central H is almost completely consumed, the convective core disappears. Then, the He-rich core contracts and heats up until the 3α reactions are activated and a new convective core appears. As usual, owing to the conversion of He into C and, later on, into O, the external border of the convective core moves forward, and more outside, a semiconvective zone forms (see [21] and references therein). This quite standard scenario drastically changes in the $Z = 10^{-10}$ model. At the beginning of the Main Sequence phase, owing to the scarcity of metals, the star is forced to burn hydrogen mainly through the pp chain, while the CNO cycle is only marginally activated. This leads to the formation of a much smaller convective core that rapidly disappears. Then, the core contracts until the central temperature is high enough that the 3α reactions take place so that primary ^{12}C is synthesized. As a

consequence, the efficiency of the CNO cycle increases. When the abundance of carbon rises above $\sim 2 \times 10^{-10}$, the CN cycle becomes the most relevant energy source and a second convective core forms. As it is well-known, core-H and He burnings are two distinct evolutionary phases in higher metallicity models. However, when the metallicity drops below a critical value, the H burning (pp chain) and the He burning (3α) may coexist. The threshold metallicity at which this uncommon event occurs is between $Z = 10^{-6}$ and $Z = 10^{-10}$, the precise value depending on the stellar mass. When the second convective core develops, the central region expands. Later on, after the central-H exhaustion, the He-rich core contracts again until the He burning is reactivated and a third convective core appears. This particular trait of the lowest metallicity model leaves a characteristic footprint in the evolutionary tracks, which are shown in Figure 2.

In Figure 3, the relation between the central temperature and density is reported. As the metallicity decreases, the central-H burning sets in at higher central temperatures and densities. Generally, the interiors of low-metallicity stars are expected to be hotter and more compact than their higher metallicity counterparts. This also influences the core-He burning, which takes place in the blue part of the Hertzsprung–Russell (HR) diagram. As a consequence, none of these low-metallicity stars experience the first dredge-up (FDU). Of note, the duration of the core-He-burning phase in the $Z = 10^{-10}$ model, which is significantly shorter than that of the two models with higher Z (see Table 1). This is essentially due to the scarce efficiency of the H-burning shell. At a higher metallicity, the shell-H burning provides a non-negligible fraction of the stellar luminosity, but in extremely metal-poor objects, most of the energy should be supplied by the central-He burning. As a result, temperature and density are higher within the core, and the He burning proceeds at a faster rate. As for the previous core-H-burning phase, the pp chain is the dominant shell-H burning channel in these metal-deficient objects.

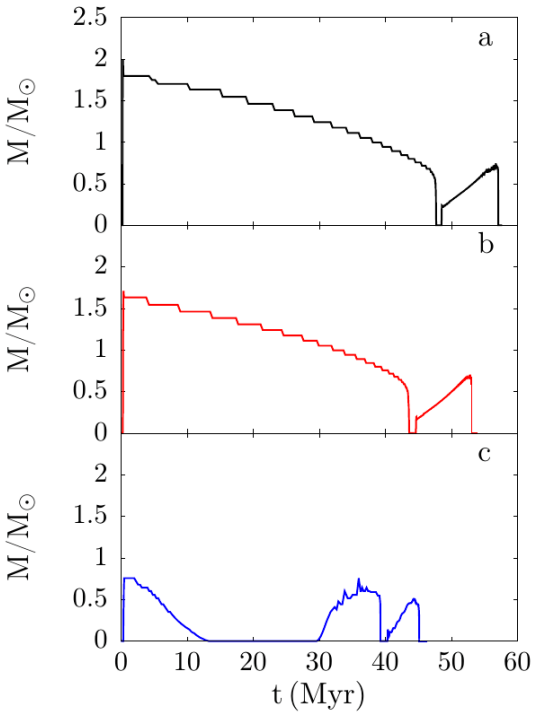

Figure 1. Mass extension of the convective cores for the three 6 $M_\odot$ models with different initial metallicities, namely $Z = 10^{-4}$ (panel **a**), $Z = 10^{-6}$ (panel **b**) and $Z = 10^{-10}$ (panel **c**).

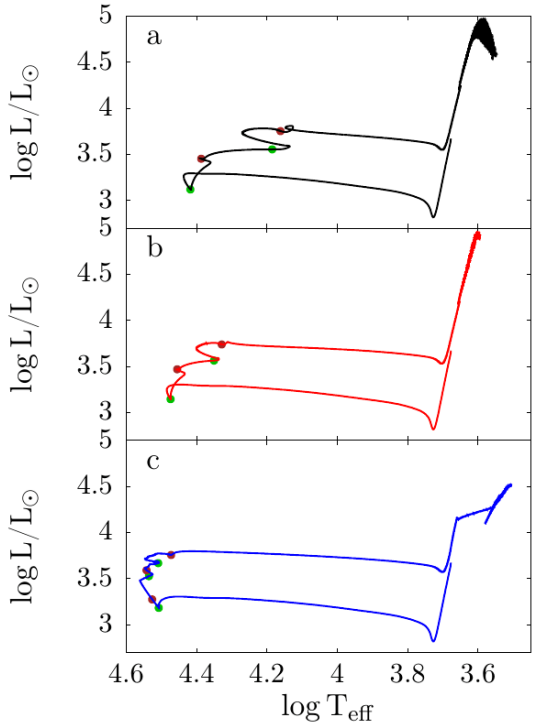

Figure 2. Hertzsprung–Russell diagrams of the three 6 $M_\odot$ models with initial metallicity $Z = 10^{-4}$ (panel **a**), $Z = 10^{-6}$ (panel **b**) and $Z = 10^{-10}$ (panel **c**). The formation and the exhaustion of each convective core are marked with green and brown dots, respectively.

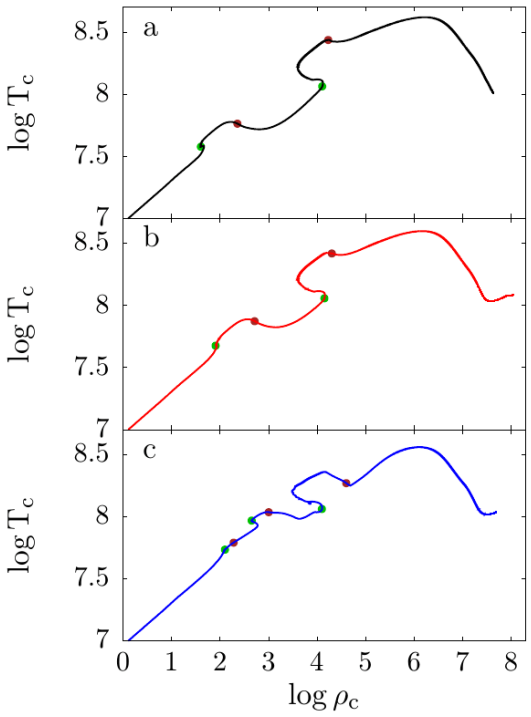

Figure 3. Evolution in the central density-central temperature plane of the three 6 $M_\odot$ models with initial metallicity $Z = 10^{-4}$ (panel **a**), $Z = 10^{-6}$ (panel **b**) and $Z = 10^{-10}$ (panel **c**). The formation and the exhaustion of each convective core are marked with green and brown dots, respectively.

2.2. The Early Asymptotic Giant Branch and the Second Dredge-Up

At the end of the central-He burning, the CO core starts contracting so that the central temperature increases. Then, electron degeneracy develops, thus preventing a further

contraction (and heating). Eventually, plasma neutrinos are efficiently produced near the center, and the most internal regions cool down. Meanwhile, He burning is active in a shell located just outside the CO core. The energy flux generated by this shell-burning powers an expansion of the external envelope, and the star becomes, for the first time, a red giant. To summarize, during this evolutionary phase, known as Early Asymptotic Giant Branch (E-AGB), the star is made of a degenerate and dense CO core, a He-burning shell surrounded by a thick He-rich intershell zone, and a rather inefficient H-burning shell surrounded by an extended H-rich convective envelope. During the ascent on the AGB, the convective envelope progressively penetrates the underlying layers. This occurrence is known as the second dredge-up (SDU), even though, at such low metallicities, this is the first time the external convection penetrates a region whose composition has been previously modified by nuclear reactions. Table 2 reports the surface abundances of some chemical species before and after the SDU. In the $Z = 10^{-4}$ model, the surface abundances of ^{12}C and ^{16}O decrease, while those of ^{13}C and ^{14}N increase, but the total number of C+N+O nuclei is almost conserved. This is a normal outcome when material processed by the CNO cycle is dredged up. A very different result is found when the metallicity is reduced. For $Z = 10^{-6}$, the ^{12}C abundance increases after the SDU, and in the $Z = 10^{-10}$ model, all the abundances of the CNO isotopes are significantly enhanced. The variation of the surface ^{12}C mass fraction in the most metal-poor model is striking, as it becomes about 5000 times higher after the SDU. This peculiarity is again a consequence of the activation of the 3α reactions in zones where H burning is active and forced to proceed at a higher temperature mainly through the pp chain rather than through the CNO cycle because of the very tiny content of the CNO nuclei. As a result, the upper portion of the He-rich core, which is penetrated by the convective envelope during the SDU, is enriched with primary carbon from the 3α reactions. Then, some of this C is partially converted into N and O. The subsequent enhancement of C+N+O in the envelope will increase the efficiency of the shell-H burning during the late part of the AGB and post-AGB phases, a fact producing profound consequences on the final fate of these stars.

Table 2. Surface chemical composition (in mass fraction) before and after the second dredge-up. The last row shows the sum C+N+O by number before and after the second dredge-up.

	$Z = 10^{-4}$		$Z = 10^{-6}$		$Z = 10^{-10}$	
	Before	**After**	**Before**	**After**	**Before**	**After**
H	7.50×10^{-1}	6.51×10^{-1}	7.50×10^{-1}	6.50×10^{-1}	7.50×10^{-1}	6.14×10^{-1}
^{4}He	2.50×10^{-1}	3.49×10^{-1}	2.50×10^{-1}	3.50×10^{-1}	2.50×10^{-1}	3.86×10^{-1}
^{12}C	1.74×10^{-5}	8.21×10^{-6}	1.74×10^{-7}	5.35×10^{-7}	1.74×10^{-11}	8.78×10^{-8}
^{13}C	1.97×10^{-7}	3.66×10^{-7}	1.97×10^{-9}	2.58×10^{-9}	1.97×10^{-13}	1.29×10^{-12}
^{14}N	4.90×10^{-6}	2.69×10^{-5}	4.90×10^{-8}	3.87×10^{-7}	4.90×10^{-12}	1.45×10^{-9}
^{16}O	4.25×10^{-5}	3.19×10^{-5}	4.25×10^{-7}	2.19×10^{-7}	4.25×10^{-11}	1.81×10^{-10}
CNO	4.46×10^{-6}	4.60×10^{-6}	4.46×10^{-8}	8.59×10^{-8}	4.46×10^{-12}	7.43×10^{-9}

2.3. Thermal Pulses, Proton Ingestion Episodes and Hot Bottom Burning

After the SDU, the He-burning shell becomes closer to the H/He discontinuity and dies down. Then, the shell-H burning restarts. As firstly shown by [22], the following evolution is characterized by recursive thermal instabilities, also called thermal pulses (TPs). In brief, during the late part of the AGB, shell-H burning provides the energy needed to supply the radiative losses from the stellar surface. While fresh helium is accumulated behind the H-burning shell, the He burning is off. However, when enough He has been piled up, the 3α reactions are activated, inducing a thermonuclear runaway (He flash). The huge amount of nuclear energy released in this way powers the formation of an extended convective region, which may mix the whole He-rich intershell. Then, a quiescent He burning sets in, while the H burning stops, and the external convection can eventually penetrate the H-exhausted core, bringing the ashes of the internal nucleosynthesis (TDU)

to the surface. This series of events repeats cyclically until the intense mass-loss affecting these bright red giant stars erodes much of the H-rich envelope. However, a pioneer work on pop III AGB stars [23] (see also [24]) found that, at variance with this well-established scenario for AGB stars of "normal" metallicity, thermal pulses are suppressed in a model of 5 $M_{\odot}$ that has $Z = 0$. More specifically, the H and He shells advance simultaneously, both experiencing uninterrupted steady burnings. In practice, because of the lack of CNO nuclei, the H burning proceeds at a rate similar to that of the He burning. According to their findings, they speculate that in massive AGB with $Z = 0$, the degenerate CO core can accrete enough mass from the overlying steady-burning shells, thus approaching the Chandrasekhar limit. As a result, these primordial AGB stars could have experienced a carbon deflagration, ending their lives as type I and 1/2 supernovae, i.e, thermonuclear supernovae, such as type Ia, but showing H in their spectra, such as type II. Later on, this scenario for metal-deficient AGB stars was substantially revised [11,17,25,26]. Indeed, due to the CNO enhancement caused by the SDU, an almost "normal" shell-H burning takes place during the late AGB, and thermal pulses are not fully suppressed. Nevertheless, their features are rather peculiar.

In panels a and b of Figure 4, we report, respectively, the H-burning and the He-burning luminosities, while in panel c, we show the evolution of the surface CNO abundances during the TP-AGB of our 6 $M_{\odot}$, $Z = 10^{-4}$ model. Similar plots, but for $Z = 10^{-6}$ and $Z = 10^{-10}$, are shown in Figures 5 and 6, respectively. The influence of the metallicity is evident here. As far as the $Z = 10^{-4}$ model is concerned, after a first series of quite normal TPs, the H-burning luminosity presents a sudden increase, the peak value being two orders of magnitude greater than its quiescent value. This peak and the others irregularly repeated in the following evolution are due to H-burning runaways triggered by proton ingestion episodes (PIEs) [11,26–28]. A PIE or H flash occurs when the convective zone powered by a thermal pulse extends beyond the H/He discontinuity. Hence, protons are rapidly brought inwards and burnt on-fly at a high temperature (150–200 MK), causing a rapid increase in the H-burning rate. Note that, in higher metallicity stars, PIEs are prevented because of the entropy barrier erected by the very efficient shell-H burning. When protons from the envelope are moved into the intershell zone and burnt at higher temperatures, the convective zone splits into two separate regions—the most internal powered by the 3α reactions and the external one dominated by the CNO cycle. The occurrence of the first PIE has profound consequences on the following evolution. First of all, the strength of the pulses, as measured by the maximum luminosity attained during the He flashes, becomes significantly higher. As a result, the subsequent TPs are always followed by TDU episodes. Consequently, the surface of the star is enriched in the products of the He burning, namely ^{12}C and ^{16}O, and H burning, mainly ^{4}He, but also ^{14}N and ^{13}C. Then, at the reactivation of the H shell, the base of the convective envelope is hot enough to partially transform ^{12}C and ^{16}O into ^{14}N. This phenomenon is known as hot bottom burning (HBB). In our $Z = 10^{-4}$ model, the maximum temperature attained during an interpulse period at the base of the convective envelope is larger than 10^8 K. The concurrent action of PIEs, TDUs and HBB leaves a characteristic footprint in the surface abundances (panel c of Figure 4). Note that HBB is active since the beginning of the TP-AGB, while TDUs start later—after 43 TPs.

Figure 5 reports the same quantities for the $Z = 10^{-6}$ model. The first part of the TP-AGB phase is similar to that of the higher metallicity model. After a few tens of TPs, a series of PIEs begins, but their effects are hampered by the lower metallicity. For about 10^5 yr, the occurrence of PIEs sustains the overall strength of the thermal pulses, and shallow dredge-up episodes take place. Then, thermal pulses become progressively weaker (see central panel in Figure 5) so that PIEs and TDUs cease. Meanwhile, the envelope composition is regulated by a moderate HBB. At the base of the convective envelope, the temperature is high enough to maintain the CNO equilibrium, and the variation of the surface composition is limited by the large dilution resulting from the deep convective mixing.

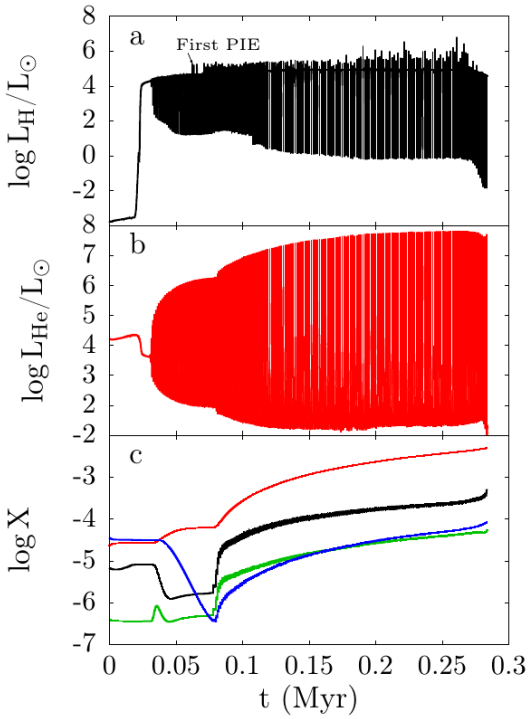

Figure 4. TP-AGB phase for the $Z = 10^{-4}$ model. Panels **a** and **b** show the evolution of the H-burning luminosity and that of the He-burning luminosity, respectively, while panel **c** those of the surface abundances (in mass fraction) of the most relevant CNO isotopes, namely: ^{12}C (black), ^{13}C (green), ^{14}N (red) and ^{16}O (blue). Time 0 is set at the beginning of the SDU.

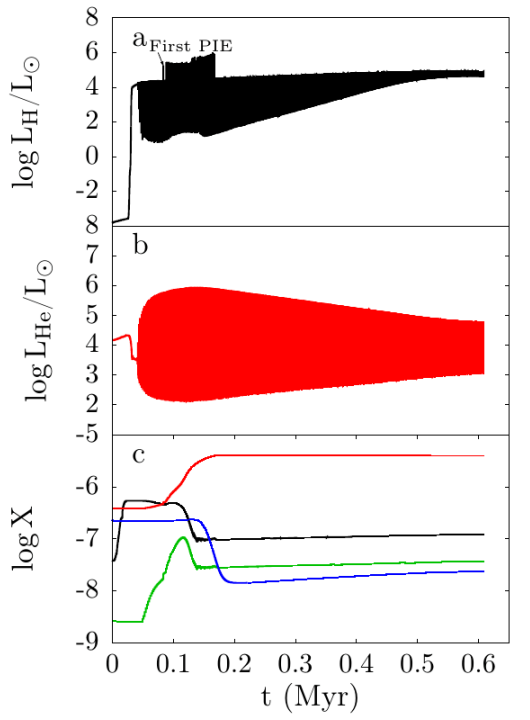

Figure 5. TP-AGB phase for the $Z = 10^{-6}$ model. Panels **a** and **b** show the evolution of the H-burning luminosity and that of the He-burning luminosity, respectively, while panel **c** those of the surface abundances (in mass fraction) of the most relevant CNO isotopes, namely: ^{12}C (black), ^{13}C (green), ^{14}N (red) and ^{16}O (blue). Time 0 is set at the beginning of the SDU.

When the model metallicity is further lowered, although some C, N and O have been dredged up by the SDU, the shell-H burning is definitely less efficient than in the more metal-rich models. Thermal pulses are not suppressed, but they are substantially weaker, and the convective zone they generate remains well far from the H/He discontinuity so that no proton ingestion episodes occur. Furthermore, the temperatures at the base of the convective envelope remain much lower during the interpulse periods. It results in a very marginal activation of the HBB. Noteworthy, in both the $Z = 10^{-6}$ and $Z = 10^{-10}$ models, as the star climbs the TP-AGB, the H burning tends to become almost stationary (see panels a in Figures 5 and 6).

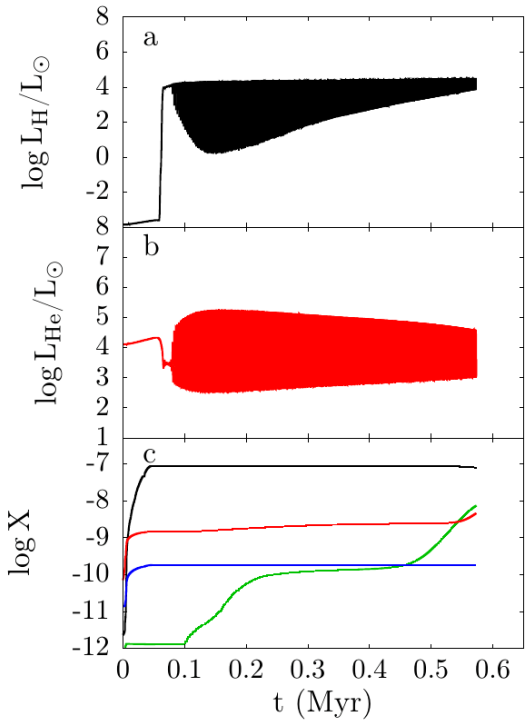

Figure 6. TP-AGB phase for the $Z = 10^{-10}$ model. Panels **a** and **b** show the evolution of the H-burning luminosity and that of the He-burning luminosity, respectively, while panel **c** those of the surface abundances (in mass fraction) of the most relevant CNO isotopes, namely: ^{12}C (black), ^{13}C (green), ^{14}N (red) and ^{16}O (blue). Time 0 is set at the beginning of the SDU.

Let us now concentrate on the nucleosynthesis of the $Z = 10^{-4}$ model, which is the only one showing sizeable modifications of the surface chemistry. Besides the CNO abundances, it is worth focusing on other isotopes, such as those belonging to the NeNa and MgAl cycles. The evolution of the surface abundances of the main isotopes involved in the NeNa cycle is reported in Figure 7. During the first part of the TP-AGB phase before the occurrence of the first PIE, the most evident variations of the Ne and Na isotopic abundances are the depletion of ^{23}Na and the corresponding enhancement of ^{20}Ne. Furthermore, ^{21}Ne is depleted, while the abundance of ^{22}Ne is only marginally affected. Note, however, that the total abundance by the number of Ne+Na is conserved. This is a consequence of the activation of the NeNa cycle at the base of the convective envelope. Indeed, after a few TPs, the temperature at the base of the external convective zone rises up to ∼100 MK. Later on, after the occurrence of the first PIE, fresh ^{22}Ne is dredged up from the intershell region. It is produced during a thermal pulse through the following chain:

$$^{14}\mathrm{N}(\alpha,\gamma)^{18}\mathrm{F}(\beta^+,\nu)^{18}\mathrm{O}(\alpha,\gamma)^{22}\mathrm{Ne}. \quad (1)$$

As a consequence of the ^{22}Ne dredge-up, the total amount of Ne+Na will increase within the stellar envelope. Then, since the onset of the first PIE, the abundances of all

the Ne and Na isotopes start increasing at the stellar surface. As usual, at the base of the external convective zone, the relative isotopic abundance ratios are tuned according to the inverses of the corresponding p-capture rates. Then, the surface composition also depends on the envelope dilution.

Similarly, the evolution of the surface abundances of the isotopes involved in the MgAl cycle (Figure 8) is due to the the synergies among HBB, PIEs and TDUs. During the first 43 TPs, only the HBB is active. Hence, the abundances of ^{25}Mg, ^{26}Al, ^{27}Al and ^{28}Si increase, while those of ^{24}Mg and ^{26}Mg decrease. After the first PIE, however, sizeable TDUs take place, and fresh Mg is dredged up from the intershell zone. This is the result of the partial conversion of ^{22}Ne into ^{25}Mg ad ^{26}Mg via the following reactions active during a thermal pulse: ^{22}Ne(α,n)^{25}Mg and ^{22}Ne(α, γ)^{26}Mg. Therefore, during the late part of the AGB phase, all the abundances of isotopes belonging to the MgAl cycle grow.

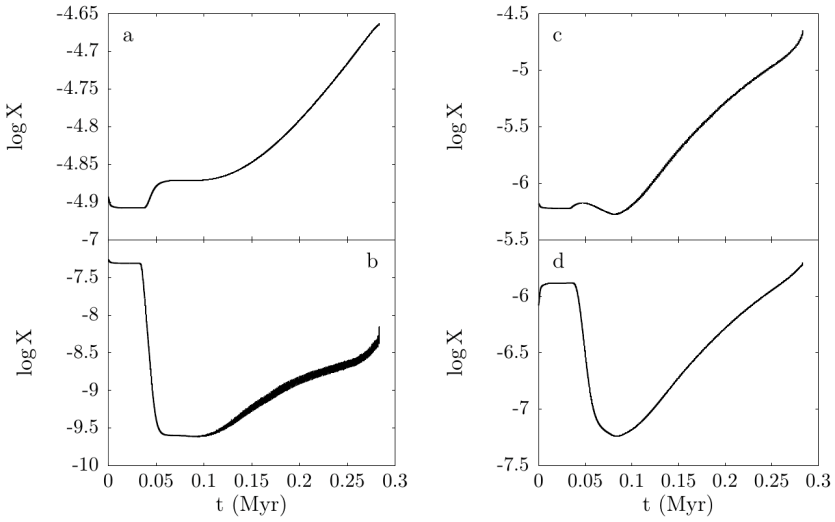

Figure 7. The activation of the NeNa cycle in the $Z = 10^{-4}$ model. The four panels show the evolution during the AGB phase of of the surface abundances (in mass fraction) of some relevant isotopes, namely: ^{20}Ne (panel **a**), ^{21}Ne (panel **b**), ^{22}Ne (panel **c**) and ^{23}Na (panel **d**). Time 0 is set at the beginning of the SDU.

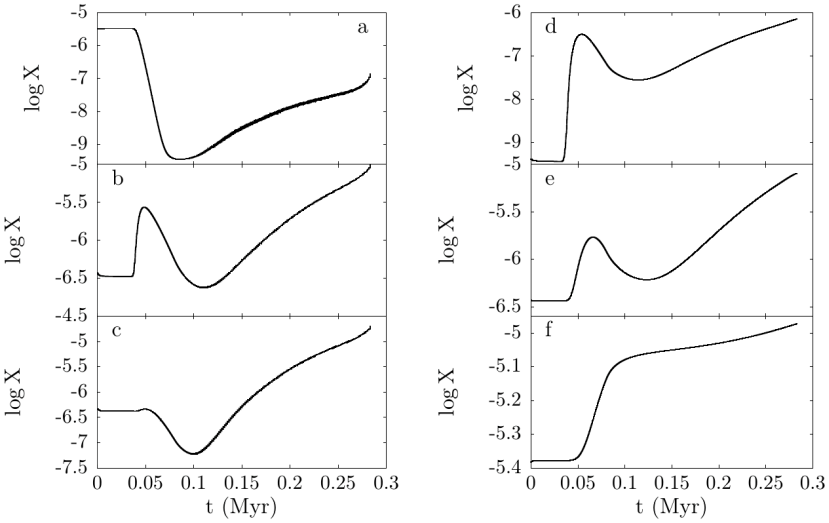

Figure 8. The activation of the MgAl cycle in the $Z = 10^{-4}$ model. The six panels show the evolution during the AGB phase of the surface abundances (in mass fraction) of some relevant isotopes, namely: ^{24}Mg (panel **a**), ^{25}Mg (panel **b**), ^{26}Mg (panel **c**), ^{26}Al (panel **d**), ^{27}Al (panel **e**) and ^{28}Si (panel **f**). Time 0 is set at the beginning of the SDU.

3. Low-Mass AGB Stars

In this section, we will analyze the evolution and nucleosynthesis of a model with $M = 2\ M_\odot$, $Y = 0.25$, and $Z = 10^{-5}$, with particular emphasis on the AGB phase. This model represents a good candidate for the primary component of binary systems hosting a CEMPs star.

3.1. From Central-H Burning to E-AGB

In spite of the low metallicity, the H- and He-burning phases are rather standard, with corresponding lifetimes of 575 Myr and 97.8 Myr. The HR diagram is shown in Figure 9. The core-H burning is driven by a weak CNO cycle, even though the pp chain provides a non-negligible contribution to the energy budget. As usual, at the beginning of the Main Sequence, a convective core develops, whose mass decreases as H is converted into ^{4}He. After ∼200 Myr, the convective core eventually disappears, and the H burning proceeds in a radiative core for a few hundreds Myr. At the central-H exhaustion, the star climbs the RGB and experiences the FDU. As a result, the surface mass fraction of C reduces (−16%), while that of N increases (+50%). Then, the He ignition occurs in a mild degenerate core, and during the following quiescent core-He burning, the model shows a wide blue loop. Later on, the star enters the AGB phase. At variance with the more massive models, these low-mass stars do not undergo a SDU, and, when the He-burning shell gets closer to the H-burning one, the He burning eventually dies down. This event marks the beginning of the TP-AGB.

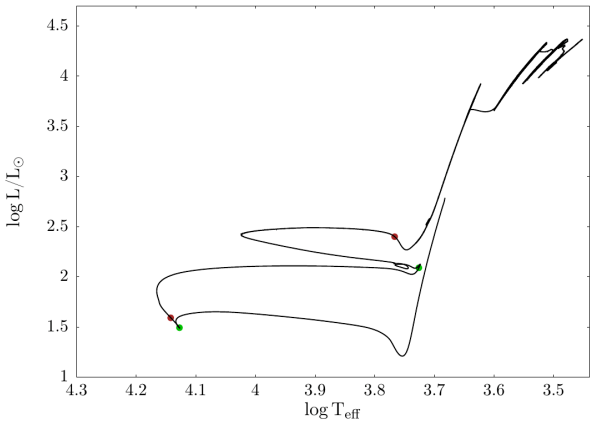

Figure 9. Hertzsprung–Russell diagram of the $M = 2\ M_\odot$, $Z = 10^{-5}$ model. Green and brown dots indicates the formation and the exhaustion of each convective core, respectively.

3.2. The TP-AGB Phase

As the H-burning shell moves outwards, fresh helium is left behind it. Then, when enough helium is accumulated, the first thermal pulse starts. A convective region develops above the He-burning shell, and ^{12}C and ^{16}O are synthesized by the 3α and ^{12}C(α, γ)^{16}O reactions, respectively. As already found in more massive stars, owing to the low metallicity, the entropy barrier provided by the shell-H burning is not very efficient. In this low-mass model, however, thermal pulses are much stronger than those found in the 6 $M_\odot$ models, and the convective region they power can easily cross the H/He discontinuity, penetrating the H-rich envelope. As a consequence, a violent PIE occurs during the second well-developed thermal pulse. It attains a luminosity peak as high as 10^{10} $L_\odot$ (see Figure 10).

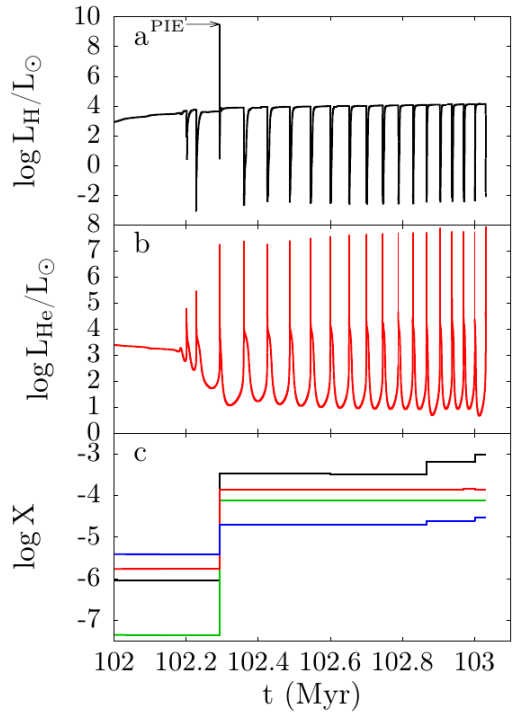

Figure 10. TP-AGB phase for the model with M = 2 $M_\odot$, $Z = 10^{-5}$. Panels **a** and **b** show the evolution of the H-burning luminosity and that of the He-burning luminosity, respectively, while panel **c** those of the surface abundances (in mass fraction) of the most relevant CNO isotopes, namely: ^{12}C (black), ^{13}C (green), ^{14}N (red) and ^{16}O (blue). Time 0 is set at the beginning of the FDU.

Note that this PIE is much stronger than those found in the more massive models and it has a major influence on the following evolution. As the H flash starts, the convective region splits into two different zones. Figure 11 shows the radiative and the adiabatic temperature gradients after the splitting. Convective regions may be easily identified by means of the Schwarzschild criterion.

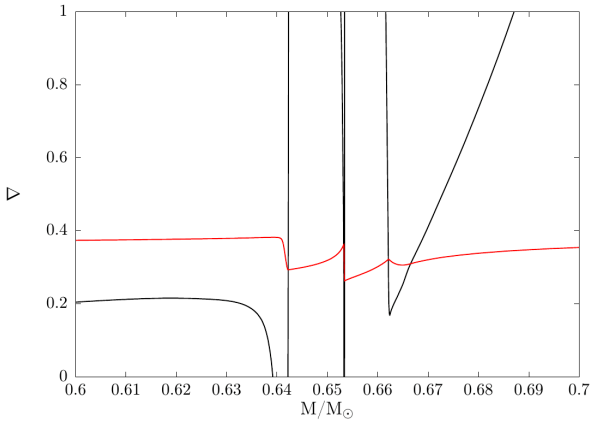

Figure 11. Radiative (black) and adiabatic (red) temperature gradients as functions of the mass coordinate during the PIE. Three convective regions can be identified: the most internal, related to the initial thermal instability, driven by the He burning; the central one, powered by the CNO cycle; the most external, corresponding to the base of the convective envelope.

Figure 12 reports the internal temperature and density profiles between the top of the CO core and the base of the H-rich envelope. Here, the three panels represent different evolutionary epochs, namely: (a) just before the occurrence of the PIE, (b) when the convective zone developed after the PIE reaches its maximum extension and (c) at the time

of the subsequent TDU episode (deepest penetration of the convective envelope). As far as the upper panel is concerned, a maximum temperature of ∼253 MK is reached at the bottom of the pulse-driven convective zone. Then, after the proton ingestion (panel b), a secondary maximum in the temperature forms. This is the layer where most of the flying protons are burnt and, in turn, where the nuclear energy release is concentrated. It coincides with the bottom of the central convective zone that powered by the H burning (green hatched area in Figure 10). Later on, the convective envelope penetrates deeply inwards (panel c), engulfing most of the region previously mixed by the central convective zone. It results in a substantial increase in surface CNO abundances so that the subsequent TP-AGB evolution is similar to that of higher metallicity AGB stars. In particular, the following TPs show a gradual increase in the He-burning luminosity peak, and, after 11 TPs not followed by TDU episodes, the surface composition starts being regularly modified by cyclic TDUs. No further PIE is found.

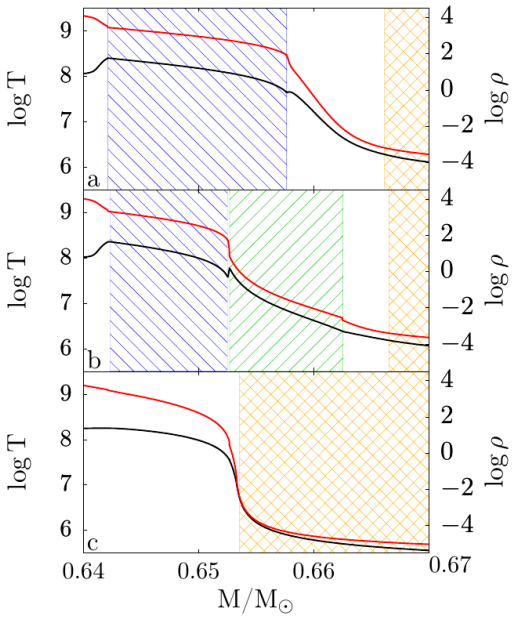

Figure 12. Temperature (black line) and density (red line) profiles in the intershell region: at the beginning of the thermal pulse but before the PIE (panel **a**); during the PIE, when the convective zone powered by the proton ingestion reaches its maximum extension (panel **b**); during the subsequent TDU episode, when the convective envelope attains its maximum inward penetration (panel **c**). In each panel, the convective zones powered by the He-shell flash and by the H-shell flash are hatched blue and green, respectively, while the convective envelope is squared orange.

3.3. The Chemistry of the Proton Ingestion Episode

Figures 13 and 14 illustrate the variations of H, ^{4}He and some CNO isotopes within the transition zone between the CO core and the bottom of the H-rich envelope. Panels a, b and c refer to the same three epochs already shown in Figure 12. Initially, the 3α reactions active at the base of the pulse-driven convective zone synthesize ^{12}C, whose mass fraction rises up to ∼0.15. As protons are ingested and the splitting of the convective zone takes place (panels b), the H mass fraction in the central convective zone suddenly rises up to ∼0.32 (at the bottom of the this region) and ∼0.38 (at its top). In addition, a substantial increase in the ^{12}C abundance and in the other CNO isotopes can be noticed in the same convective zone. Then, the convective envelope dredges up the isotopes produced in the central region (panels c). After the PIE, the metallicity in the envelope rises up to $Z \sim 6 \times 10^{-4}$, mostly because of the dredged carbon and nitrogen. The surface composition before and after this dredge-up episode is detailed in Table 3.

An interesting feature of this star is the significant lithium production occurring in the intershell zone at the PIE epoch. Figure 15 reports ^{7}Li (black), ^{7}Be (red) and ^{11}B (blue)

abundance profiles in the relevant layers. The three panels are as in the previous plots. During the PIE, ^{3}He is caught by convection and moved inwards, where ^{7}Be is produced by ^{3}He$(\alpha,\gamma)^{7}$Be. Since proton captures on ^{12}C and ^{13}C are much faster than those on ^{7}Be, the latter is only marginally destroyed. In practice, most of the engulfed ^{3}He is transformed into ^{7}Be. Then, on a longer timescale, ^{7}Be slowly decays into ^{7}Li, and both can capture α particles, thus producing ^{11}B. Later on, after the subsequent TDU episode, the stellar surface should eventually become Li-rich.

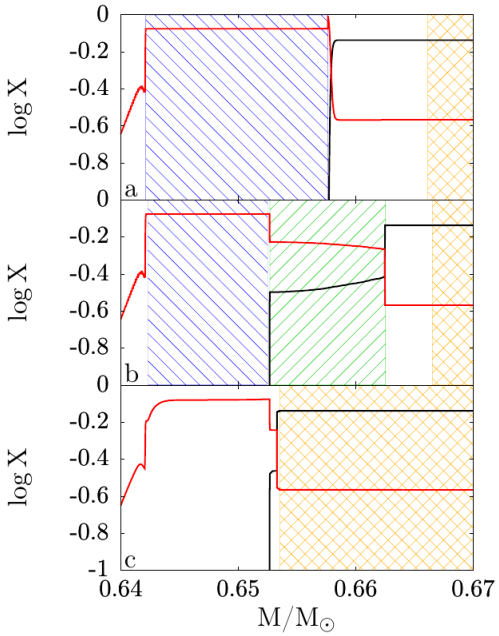

Figure 13. Profiles of various chemical abundances (in mass fraction) within the intershell region: H (black) and ^{4}He (red). The three panels and the hatched areas are as in Figure 12.

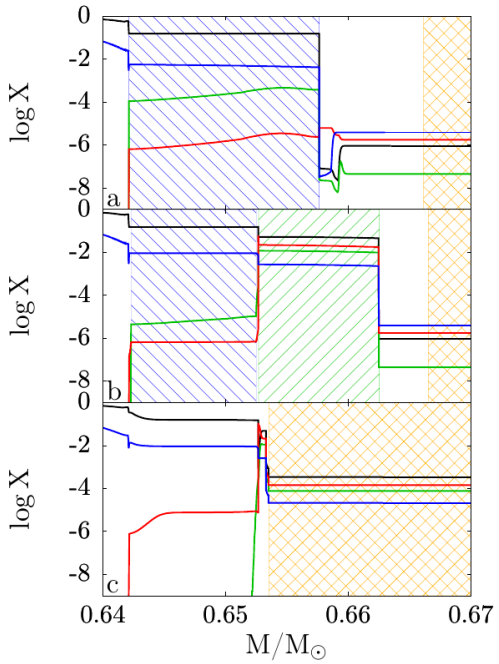

Figure 14. Profiles of various chemical abundances (in mass fraction) within the intershell region: ^{12}C (black), ^{13}C (green), ^{14}N (red) and ^{16}O (blue). The three panels and the hatched areas are as in Figure 12.

Table 3. Surface chemical composition (in mass fraction) before the PIE and after the subsequent TDU.

	Before	After		Before	After
H	7.30×10^{-1}	7.27×10^{-1}	^{20}Ne	1.28×10^{-6}	1.28×10^{-6}
^{4}He	2.70×10^{-1}	2.75×10^{-1}	^{21}Ne	1.06×10^{-8}	1.05×10^{-8}
^{12}C	9.12×10^{-7}	3.40×10^{-4}	^{22}Ne	8.36×10^{-8}	1.12×10^{-7}
^{13}C	4.42×10^{-8}	7.66×10^{-5}	^{23}Na	5.70×10^{-8}	5.75×10^{-8}
^{14}N	1.75×10^{-6}	1.44×10^{-4}	^{24}Mg	3.11×10^{-7}	3.11×10^{-7}
^{16}O	3.87×10^{-6}	2.14×10^{-5}	^{25}Mg	3.85×10^{-8}	3.86×10^{-8}
^{7}Li	2.24×10^{-13}	5.84×10^{-9}	^{26}Mg	4.75×10^{-8}	4.79×10^{-8}
^{7}Be	4.18×10^{-39}	3.75×10^{-21}	^{26}Al	2.60×10^{-13}	9.38×10^{-12}
^{11}B	7.09×10^{-17}	5.75×10^{-16}	^{27}Al	3.69×10^{-8}	3.68×10^{-8}
^{15}N	5.71×10^{-10}	3.06×10^{-9}	^{28}Si	4.14×10^{-7}	4.17×10^{-7}
^{17}O	1.90×10^{-8}	7.80×10^{-8}	^{29}Si	6.49×10^{-23}	4.99×10^{-9}
^{18}O	5.48×10^{-9}	5.45×10^{-9}	^{56}Fe	7.17×10^{-7}	7.14×10^{-7}
^{19}F	3.34×10^{-10}	3.39×10^{-10}	^{56}Ni to ^{208}Pb	4.99×10^{-7}	5.02×10^{-7}

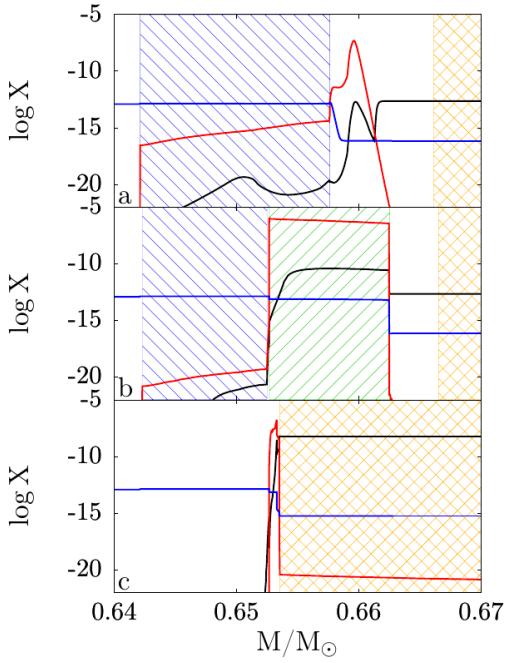

Figure 15. Profiles of various chemical abundances (in mass fraction) within the intershell region: ^{7}Li (black), ^{7}Be (red) and ^{11}B (blue). The three panels and the hatched areas are as in Figure 12.

4. Conclusions

In this paper, we have reviewed the evolution and the nucleosynthesis of metal-poor and EMP stars ($Z \leq 10^{-4}$) with a mass low enough to skip the activation of central-C burning ($M < M_{up}$).

In general, the scarcity of CNO isotopes implies a higher temperature and density in the regions where H burning takes place. In the most metal-poor stars, the temperature may be large enough for the activation of the 3α reactions. Then, primary carbon is synthesized and, in the case of dredge-up events, the efficiency of the CNO cycle can be improved. As a whole, these occurrences have profound consequences on both the evolution and the nucleosynthesis.

In the more massive objects (5–7 $M_{\odot}$), the SDU causes a significant increment in surface C (and other CNO isotopes). For instance, in the 6 $M_{\odot}$ model with $Z = 10^{-10}$, we find that the C and N overabundances after the SDU are [C/Fe] = 3.7 and [N/Fe] = 2.5, respectively. Then, if the metallicity is lower than 10^{-6}, rather weak thermal pulses develop

when the He-burning shell approaches the border of the H-exhausted core. Therefore, no TDU is expected in these EMP stars, and their surface composition is only marginally modified by HBB. Since their lifetime is quite short (about 40 Myr for a 6 $M_{\odot}$), they could be responsible for the C enhancement shown by some CEMP (no-s) stars.

On the contrary, no SDU occurs in EMP stellar models with smaller masses. However, at the beginning of the TP-AGB phase, they experience a violent PIE followed by a deep TDU, whose major consequence is the huge increase in surface CNO abundances. Then, the subsequent evolution is similar to that of more metal-rich low-mass AGB models. In particular, s-process nucleosynthesis is expected to take place in the intershell region, mainly driven by the activation of the $^{13}C(\alpha, n)^{16}O$ reaction during the interpulse period. This s-process-enriched material is dredged up by recursive TDU episodes. Thus, large overabundances of carbon and s-process isotopes are expected to appear in the envelope of these objects. In binary systems, this material can be eventually transferred to a smaller and less evolved companion by Roche lobe overflow or wind accretion in agreement with the composition observed in CEMP (s-rich) stars.

Author Contributions: Conceptualization, O.S.; Formal analysis, M.C. and L.P.; Investigation, L.P. and O.S.; Methodology, L.P. and O.S.; Project administration, O.S.; Software, L.P.; Supervision, L.P. and O.S.; Validation, L.P. and O.S.; writing—review and editing, M.C. and O.S. All authors have read and agreed to the published version of the manuscript.

Funding: The PhD fellow of M. Cirillo is partially supported by the SKA project.

Institutional Review Board Statement: Not applicable.

Informed Consent Statement: Not applicable.

Acknowledgments: This work is part of the PhD thesis project of Mario Cirillo. He is enrolled in the XXXV cycle of the Astronomy, Astrophysics and Space Science PhD program, a joint initiative of Sapienza University (Rome), Tor Vergata University (Rome), and Italian National Institute of Astrophysics (INAF).

Conflicts of Interest: The authors declare no conflict of interest.

References

1. Zuo, W.; Du, C.; Jing, Y.; Gu, J.; Newberg, H.J.; Wu, Z.; Ma, J.; Zhou, X. The Stellar Metallicity Distribution of the Galactic Halo Based on SCUSS and SDSS Data. *Astrophys. J.* **2017**, *841*, 59. [CrossRef]
2. Marengo, M.; Mullen, J.; Neeley, J.R.; Fabrizio, M.; Marrese, P.M.; Bono, G.; Braga, V.F.; Magurno, D.; Crestani, J.; Fiorentino, G.; et al. Metallicity Distribution of Galactic Halo Field RR Lyræ, and the Effect of Metallicity on Their Pulsation Properties. *arXiv* **2021**, arXiv:2006.09625.
3. Glover, S.C.O.; Clark, P.C.; Greif, T.H.; Johnson, J.L.; Bromm, V.; Klessen, R.S.; Stacy, A. Open questions in the study of population III star formation. In *Low-Metallicity Star Formation: From the First Stars to Dwarf Galaxies*; Hunt, L.K., Madden, S.C., Schneider, R., Eds.; Cambridge University Press: Cambridge, UK, 2009; Volume 4, pp. 3–17. [CrossRef]
4. Saslaw, W.C.; Zipoy, D. Molecular Hydrogen in Pre-galactic Gas Clouds. *Nature* **1967**, *216*, 976–978. [CrossRef]
5. Palla, F.; Salpeter, E.E.; Stahler, S.W. Primordial star formation—The role of molecular hydrogen. *Astrophys. J.* **1983**, *271*, 632–641. [CrossRef]
6. Nakamura, F.; Umemura, M. The Stellar Initial Mass Function in Primordial Galaxies. *Astrophys. J.* **2002**, *569*, 549–557. [CrossRef]
7. Nagakura, T.; Omukai, K. Formation of Population III stars in fossil HII regions: Significance of HD. *Mon. Not. R. Astron. Soc.* **2005**, *364*, 1378–1386. [CrossRef]
8. Johnson, J.L.; Bromm, V. The cooling of shock-compressed primordial gas. *Mon. Not. R. Astron. Soc.* **2006**, *366*, 247–256. [CrossRef]
9. Mattsson, L. The origin of carbon: Low-mass stars and an evolving, initially top-heavy IMF? *Astron. Astrophys.* **2010**, *515*, A68. [CrossRef]
10. Bisterzo, S.; Gallino, R.; Straniero, O.; Cristallo, S.; Käppeler, F. The s-process in low-metallicity stars—II. Interpretation of high-resolution spectroscopic observations with asymptotic giant branch models. *Mon. Not. R. Astron. Soc.* **2011**, *418*, 284–319. [CrossRef]
11. Chieffi, A.; Domínguez, I.; Limongi, M.; Straniero, O. Evolution and Nucleosynthesis of Zero-Metal Intermediate-Mass Stars. *Astrophys. J.* **2001**, *554*, 1159–1174. [CrossRef]
12. Straniero, O.; Gallino, R.; Cristallo, S. s process in low-mass asymptotic giant branch stars. *Nucl. Phys. A* **2006**, *777*, 311–339. [CrossRef]

13. Piersanti, L.; Cristallo, S.; Straniero, O. The Effects of Rotation on s-process Nucleosynthesis in Asymptotic Giant Branch Stars. *Astrophys. J.* **2013**, *774*, 98. [CrossRef]
14. Straniero, O.; Dominguez, I.; Piersanti, L.; Giannotti, M.; Mirizzi, A. The Initial Mass-Final Luminosity Relation of Type II Supernova Progenitors: Hints of New Physics? *Astrophys. J.* **2019**, *881*, 158. [CrossRef]
15. Stancliffe, R.J. Does simultaneous solution matter for stellar evolution codes? *Mon. Not. R. Astron. Soc.* **2006**, *370*, 1817–1822. [CrossRef]
16. Campbell, S.W.; Lattanzio, J.C. Evolution and nucleosynthesis of extremely metal-poor and metal-free low- and intermediate-mass stars. I. Stellar yield tables and the CEMPs. *Astron. Astrophys.* **2008**, *490*, 769–776. [CrossRef]
17. Suda, T.; Fujimoto, M.Y. Evolution of low- and intermediate-mass stars with [Fe/H] <= −2.5. *Mon. Not. R. Astron. Soc.* **2010**, *405*, 177–193. [CrossRef]
18. Iwamoto, N. Evolution and Nucleosynthesis in Extremely Metal-Poor, Asymptotic Giant Branch Stars. *Publ. Astron. Soc. Aust.* **2009**, *26*, 145–152. [CrossRef]
19. Gil-Pons, P.; Doherty, C.L.; Gutiérrez, J.; Campbell, S.W.; Siess, L.; Lattanzio, J.C. Nucleosynthetic yields of Z = 10^{-5} intermediate-mass stars. *Astron. Astrophys.* **2021**, *645*, A10. [CrossRef]
20. Ventura, P.; Dell'Agli, F.; Romano, D.; Tosi, S.; Limongi, M.; Chieffi, A.; Castellani, M.; Tailo, M.; Lugaro, M.; Marini, E.; et al. Gas and dust from extremely metal-poor AGB stars. *Astron. Astrophys.* **2021**, *655*, A6. [CrossRef]
21. Straniero, O.; Domínguez, I.; Imbriani, G.; Piersanti, L. The Chemical Composition of White Dwarfs as a Test of Convective Efficiency during Core Helium Burning. *Astrophys. J.* **2003**, *583*, 878–884. [CrossRef]
22. Schwarzschild, M.; Härm, R. Thermal Instability in Non-Degenerate Stars. *Astrophys. J.* **1965**, *142*, 855. [CrossRef]
23. Chieffi, A.; Tornambe, A. On the evolution of an intermediate-mass zero-metal star which does not experience thermal instabilities during the double shell burning phase. *Astrophys. J.* **1984**, *287*, 745–748. [CrossRef]
24. Fujimoto, M.Y.; Iben, I.J.; Chieffi, A.; Tornambe, A. Hydrogen and helium burning in zero-metal asymptotic giant branch stars and the existence of thresholds (in core mass and CNO abundance) for the occurrence of helium shell flashes. *Astrophys. J.* **1984**, *287*, 749–760. [CrossRef]
25. Dominguez, I.; Straniero, O.; Limongi, M.; Chieffi, A. Do zero metals intermediate mass stars experience thermal pulses? *arXiv* **2000**, arXiv:astro-ph/astro-ph/9912425.
26. Lau, H.H.B.; Stancliffe, R.J.; Tout, C.A. The evolution of low-metallicity asymptotic giant branch stars and the formation of carbon-enhanced metal-poor stars. *Mon. Not. R. Astron. Soc.* **2009**, *396*, 1046–1057. [CrossRef]
27. Suda, T.; Aikawa, M.; Machida, M.N.; Fujimoto, M.Y.; Iben, I.J. Is HE 0107-5240 A Primordial Star? The Characteristics of Extremely Metal-Poor Carbon-Rich Stars. *Astrophys. J.* **2004**, *611*, 476–493. [CrossRef]
28. Cristallo, S.; Straniero, O.; Lederer, M.T.; Aringer, B. Molecular Opacities for Low-Mass Metal-poor AGB Stars Undergoing the Third Dredge-up. *Astrophys. J.* **2007**, *667*, 489–496. [CrossRef]